



HAL
open science

Interaction of a Coastal Kelvin Wave with the Mean State in the Gulf Stream Separation Area

Sabine Février, Jérôme Sirven, Christophe Herbaut

► **To cite this version:**

Sabine Février, Jérôme Sirven, Christophe Herbaut. Interaction of a Coastal Kelvin Wave with the Mean State in the Gulf Stream Separation Area. *Journal of Physical Oceanography*, 2007, 37 (6), pp.1429-1444. 10.1175/JPO3062.1 . hal-00164663

HAL Id: hal-00164663

<https://hal.science/hal-00164663>

Submitted on 10 Jun 2021

HAL is a multi-disciplinary open access archive for the deposit and dissemination of scientific research documents, whether they are published or not. The documents may come from teaching and research institutions in France or abroad, or from public or private research centers.

L'archive ouverte pluridisciplinaire **HAL**, est destinée au dépôt et à la diffusion de documents scientifiques de niveau recherche, publiés ou non, émanant des établissements d'enseignement et de recherche français ou étrangers, des laboratoires publics ou privés.

Interaction of a Coastal Kelvin Wave with the Mean State in the Gulf Stream Separation Area

SABINE FÉVRIER, JÉRÔME SIRVEN, AND CHRISTOPHE HERBAUT

LOCEAN: MNHN/IPSL/CNRS/IRD/UPMC, Université Pierre et Marie Curie, Paris, France

(Manuscript received 31 March 2006, in final form 3 August 2006)

ABSTRACT

The interaction of a coastal Kelvin wave with the mean state in the Gulf Stream separation area is studied using a hierarchy of numerical models including both low- and high-resolution 2.5-layer models and a coarse-resolution ocean general circulation model (OGCM) in a simple configuration. When the Kelvin front reaches the separation area in the low-resolution 2.5-layer model, an anomaly of opposite sign emerges and remains in the upper layer of the separation area. The mechanism leading to its buildup is the following: the variations of thickness in the active midlayer due to the propagation of the Kelvin wave induce current variations that act as a source of thickness anomalies for the upper layer (negative feedback). This source term is proportional to the mean vorticity gradient. The latter therefore must be large enough to obtain a significant response, which explains why this phenomenon occurs only in the separation area. The anomaly remains in the separation area because the advection by the mean zonal current is balanced by the current anomalies due to the variations of thickness in the surface layer. A very similar response is obtained in the high-resolution case and with the OGCM; thus, the mechanism leading to this evolution seems also largely independent of the model. However, in the OGCM, the surface current is sufficiently strong to advect the anomaly in the surface layers (above 200-m depth). Note finally that these anomalies do not prevent the Kelvin waves from pursuing their travel southward and then eastward toward the eastern boundary where Rossby waves are radiated. Numerous recent results based on this adjustment mechanism therefore would be robust.

1. Introduction

Both paleoclimatic records and model simulations suggest that the meridional overturning circulation (MOC) might experience large and sometimes abrupt changes (e.g., Broecker and Denton 1989; Manabe and Stouffer 1994). Studies based on climate models indicate that this variability would be enhanced in a broad frequency range from 10 to 100 yr. Even though the mechanisms leading to this increase of the variability are largely model dependent, it is believed that it would be controlled on annual and interannual time scales by wind stress forcing (e.g., Dong and Sutton 2001), while buoyancy forcing would dominate on decadal and longer time scales (e.g., Eden and Willebrand 2001).

A source of buoyancy forcing is deep-water production, which occurs at high latitudes in the North Atlantic Ocean. However, the links between deep-water production and MOC variability are poorly understood, with observations and models giving contrasting results (Mauritzen and Häkkinen 1999; Schott et al. 2004). In simple models, buoyancy forcing can be easily prescribed and the response of the ocean studied, even though possible feedbacks are neglected. Wajsowicz and Gill (1986) and Kawase (1987) showed that the ocean adjustment is through Kelvin waves, which, in a few months, propagate anticlockwise toward the eastern boundary where they generate Rossby waves that radiate into the ocean interior, with a time scale of several years at high latitudes. Johnson and Marshall (2002, 2004) showed that the equator limits the response of the ocean in the Southern Hemisphere on decadal and shorter time scales: it thus acts as a low-pass filter on the MOC variability. Deshayes and Frankignoul (2005) investigated the spectral characteristics of the MOC with a similar model and found that

Corresponding author address: Dr. Sabine Févriér, LOCEAN, Université Pierre et Marie Curie, Tour 45, étage 4, CC 100, 4 place Jussieu, 75252 Paris CEDEX 05, France.
E-mail: sabine.fevrier@lodyc.jussieu.fr

the thermocline depth response shows a red spectrum with no prevailing time scale.

In these studies of the ocean adjustment to buoyancy forcing (Kawase 1987; Huang et al. 2000; Johnson and Marshall 2002; Johnson and Marshall 2004; Deshayes and Frankignoul 2005), the role of wind stress is neglected and the basic state of the ocean was assumed to be at rest. It is not obvious that this approximation is without consequences. This paper investigates this issue, focusing on the coastal Kelvin wave crossing the region where the Gulf Stream separates from the coast.

In this region, the warm, salty Gulf Stream crosses over the cold, fresh deep western boundary current (DWBC). Complex interactions between the subtropical and subpolar gyres thus occur there. These interactions can mainly occur in the separation and recirculation area, as in Spall (1996a,b). Using a regional primitive equation model, he found that the DWBC split in two branches, one flowing southward along the western coast and the other flowing eastward under the Gulf Stream. This branch could participate to the recirculating gyre. He then established that a large amplitude, internal oscillation of decadal scale could appear. It resulted from feedbacks between the Gulf Stream, the upper branch of the DWBC, and the recirculation gyres by means of activation or inhibition of eddy fluxes.

The damped oscillating mode found by Herbaut et al. (2002, hereinafter HSF) is another example of an oscillation for which the separation area plays a prominent role. However, the mechanism suggested by these authors does not depend on the local eddy flux dynamics. Indeed, they showed that temperature anomalies could form in the Gulf Stream separation area, then be advected by the mean current toward the subpolar gyre. These anomalies affect the thermohaline circulation, which would produce new temperature anomalies of *opposite sign* and weaker amplitude in the initial area of formation of the anomalies, generating the oscillation. Moreover, propagation of temperature anomalies (recalling coastal Kelvin wave propagation) were identified along the northern and western coast in HSF, the sign reversal seeming to occur after these anomalies have propagated south to the separation area.

The results of HSF suggest that the anomalies generated by buoyancy forcing in the subpolar gyre may interact with the mean state. In this study we analyze the mechanism of this interaction. Our approach is based on a hierarchy of numerical models: a 2.5-layer model in a low- and high-resolution setup and a coarse-resolution GCM in a simple configuration. The high-resolution 2.5-layer model allows one to resolve the eddies while the GCM simulates a more realistic stratification. For all numerical experiments, density anomalies

are prescribed in the northernmost part of a two-gyre oceanic basin where they generate Kelvin waves. Their impact on the area where the Gulf Stream separates from the coast is then studied.

The paper is organized as follows. Results obtained in the experiments made with a low-resolution 2.5-layer model are presented in section 2 and their mechanisms are described in section 3. Whether these results are robust when eddies are resolved is studied in section 4. The GCM results are presented in section 5 and compared with those of the 2.5-layer models. Discussion and conclusions are given in section 6.

2. Response in a low-resolution 2.5-layer model

a. Description of the model

The model is a reduced-gravity model with two active layers whose mean thicknesses are 800 m (for the surface layer) and 900 m [the same values as in Spall (1996a,b)]. They are above an infinite layer at rest. The density in each layer is constant. The model predicts the thickness and the velocity for the surface layer (h_1 and \mathbf{v}_1) and for the midlayer (h_2 and \mathbf{v}_2). It modifies and simplifies a previous model, which is fully described in Sirven (1996).

The momentum conservation equations are

$$\frac{\partial \mathbf{v}_i}{\partial t} + (\text{curl} \mathbf{v}_i + f) \mathbf{n} \times \mathbf{v}_i = -\text{grad}(\alpha_i b h_1 + b h_2 + \mathbf{v}_i^2/2) + \nu \Delta_H \mathbf{v}_i + \frac{\boldsymbol{\tau}_{i-1} - \boldsymbol{\tau}_i}{h_i}, \quad (1)$$

where $i = 1$ (upper layer) or $i = 2$ (midlayer) and \mathbf{n} is a vector normal to the earth's surface. The reduced gravity b is equal to 0.004 m s^{-2} (note that the density difference between each neighboring layer is constant). The two coefficients $\alpha_1 = 2$ and $\alpha_2 = 1$ allow one to account for the pressure difference between the two active layers. The surface wind stress is $\boldsymbol{\tau}_0$ and the Reynolds stress at the interface is $\boldsymbol{\tau}_1 = -k(\mathbf{v}_2 - \mathbf{v}_1)$. There is no stress between the midlayer and the still deeper layer, $\boldsymbol{\tau}_2 = 0$.

The mass conservation equations are

$$\frac{\partial h_i}{\partial t} + \text{div}(h_i \mathbf{v}_i) = 0. \quad (2)$$

Mass exchanges may be introduced if it is wanted.

The equations for the potential vorticities $q_i = (\zeta_i + f)/h_i$ are deduced from (1) and (2):

$$\frac{d}{dt} q_i = \frac{1}{h_i} \text{curl} \left(\frac{\boldsymbol{\tau}_{i-1} - \boldsymbol{\tau}_i}{h_i} + \nu \Delta_H \mathbf{v}_i \right) \quad (3)$$

(d/dt is the Lagrangian derivative and ζ_i is the relative vorticity in layer i). In the upper layer the wind stress is

TABLE 1. Main characteristics of the different models.

	2.5-layer model (low resolution)	2.5-layer model (high resolution)	OGCM
Resolution	$1^\circ \times 1^\circ$	$(1/6)^\circ \times (1/6)^\circ$	$1^\circ \times 1^\circ$
Domain	$60^\circ\text{W}-0^\circ$ $15^\circ-55^\circ\text{N}$	$60^\circ-10^\circ\text{W}$ $20^\circ-50^\circ\text{N}$	$60^\circ\text{W}-0^\circ$ $0^\circ-60^\circ\text{N}$
Layers	800 + 900 m	800 + 900 m	10 over 4000 m
Reduced gravity	0.004 m s^{-2}	0.004 m s^{-2}	
Dissipation	$\nu = 2000 \text{ m}^2 \text{ s}^{-1}$ $k = 8 \times 10^{-5} \text{ m s}^{-1}$	$\nu = 100 \text{ m}^2 \text{ s}^{-1}$ $k = 8 \times 10^{-5} \text{ m s}^{-1}$	Horizontal: $10^4 \text{ m}^2 \text{ s}^{-1}$ Vertical: $10^{-3} \text{ m}^2 \text{ s}^{-1}$
Diffusivity			Horizontal: $10^3 \text{ m}^2 \text{ s}^{-1}$ Vertical: $10^{-4} \text{ m}^2 \text{ s}^{-1}$

large, so potential vorticity is not conserved. In the mid-layer, the potential vorticity is conserved when the friction and the dissipation are negligible, hence everywhere except near the boundaries.

The basin extends from 15° to 55°N and from 60°W to 0° . The equations are solved by finite differences on a C mesh on the sphere, the mesh size being equal to 1° in both zonal and meridional directions. The spatial scheme follows Sadourny (1975) and thus preserves enstrophy. No-slip boundary conditions are applied and the gradients of h_1 and h_2 are assumed to vanish perpendicularly to the boundary. There is no added dissipation in the continuity equations and mass is conserved by the numerical scheme. The time integration is performed using a leapfrog scheme with a time step of 1 h. The viscosity coefficient ν is $2000 \text{ m}^2 \text{ s}^{-1}$ and the friction coefficient k is $8 \times 10^{-5} \text{ m s}^{-1}$ (cf. Table 1).

A 100-yr simulation has been performed with the wind stress τ_0 shown in Fig. 1; the corresponding stationary state, which is obtained at the end of the integration, is displayed in Fig. 2. The gradient of the surface layer thickness (upper and top-left panels) is strongest around 35°N where the wind stress curl vanishes. The variations of h_1 are partly compensated by those of h_2 (upper and bottom-left panels) so that the midlayer depth is nearly constant. This model crudely mimics the front that separates northern heavy waters from southern lighter waters in the ocean. The potential vorticity in the surface layer (top-right panel) also shows a strong gradient around 35°N , which is closely linked to the variations of h_1 . On the contrary, it is well homogenized in the midlayer (bottom-right panel).

b. Response of the model

The deep-water formation may be represented in various ways in a layer model. A possibility is to prescribe mass fluxes between the layers [adding a supplementary term in the mass conserving equations (2), as in Kawase (1987) or Huang et al. (2000)]. An alternative consists of applying an initial thickness anomaly, then letting the system evolve. We present results ob-

tained with the second approach because of its simplicity. Experiments with prescribed flux led to comparable results; they are briefly discussed below.

Two 1-yr experiments are performed based on the previous state. In the first one, a negative thickness anomaly of Gaussian pattern is applied in the active layers along the northern boundary, whereas there is no anomaly in the second one (the latter is hereinafter called the “control experiment”). The Gaussian peaks at -400 m at 54°N , 27.5°W . Inside the domain extending over 2.5° from this point, the mean value of the

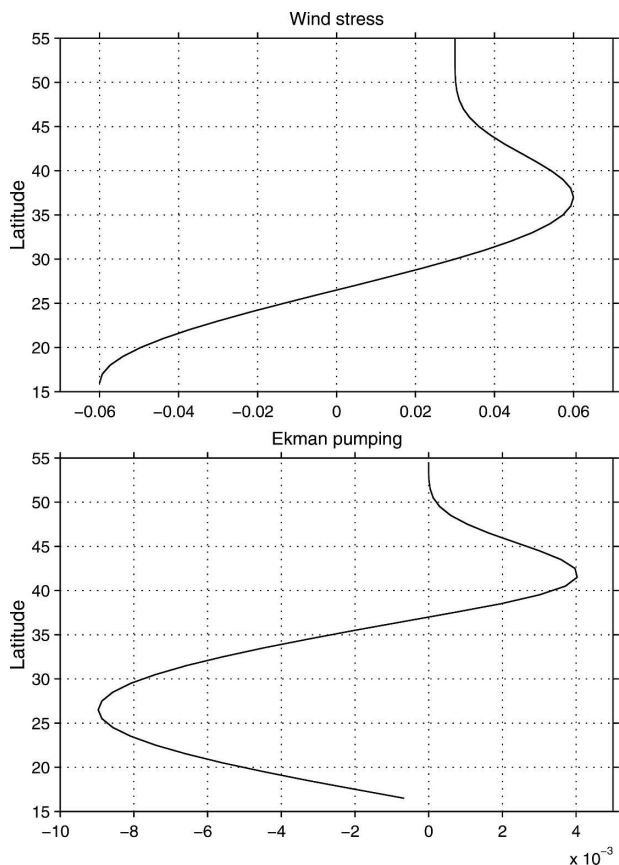


FIG. 1. Wind stress ($\text{m}^{-1} \text{ s}^{-2}$) and Ekman pumping ($\text{m}^{-2} \text{ s}^{-2}$) used in the experiments performed with the 2.5-layer model.

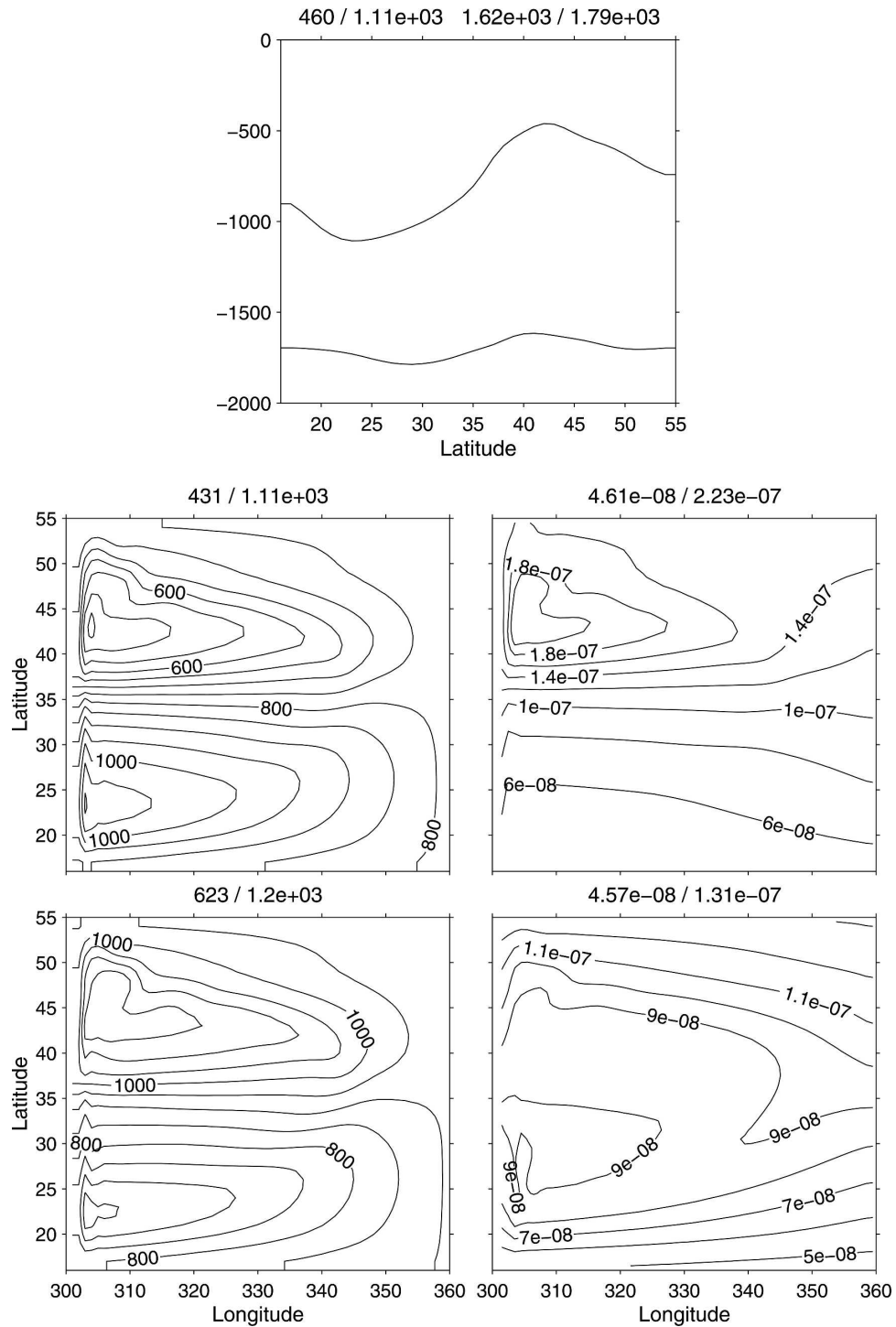


FIG. 2. Mean state of the 2.5-layer model. (top) The depth of each layer along the western side. The depths of the (middle left) first and (bottom left) second layers (m) and the potential vorticity in the (middle right) first and (bottom right) second layers ($\text{m}^{-1} \text{s}^{-1}$). Maxima and minima are indicated above each plot.

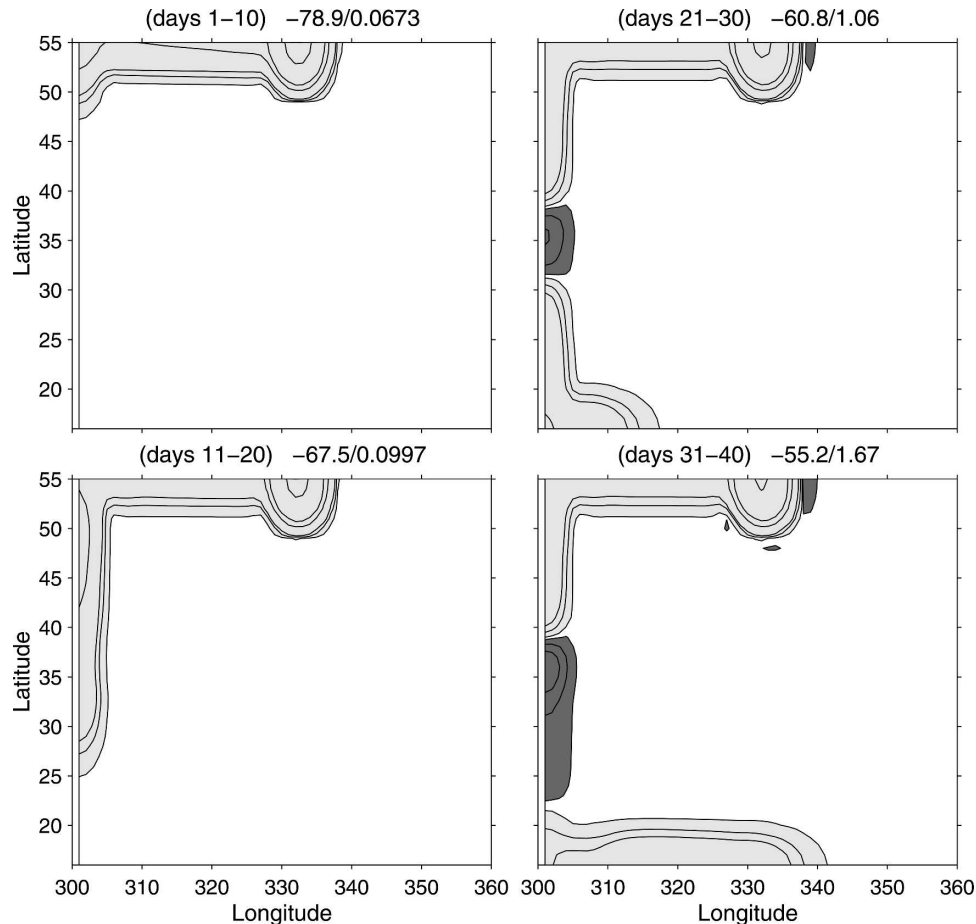


FIG. 3. Anomalies of h_1 in the 2.5-layer model (low resolution) at different times; (days i – j) means that an average from day i to day j is made. The 0 level is not indicated. The areas in dark gray are bounded by the isoline $+0.1$ m and contain isolines $+0.5$ and $+1$ m. The areas in light gray are bounded by the isoline -0.1 m and contain isolines -0.5 , -1 , -5 , -10 , -50 , and -100 m.

anomaly is about -60 m; beyond, its amplitude does not exceed 1 m.

The anomalies are defined as the differences between these two experiments. The initial anomaly quickly flattens: after one day of integration the peak reduces to 135 m and after five days to 85 m. Experiments with various initial anomalies showed that their decrease rate does not depend on their initial amplitude. The anomaly generates in both layers a coastal wave that propagates westward. Its amplitude does not exceed 1 – 2 m (Figs. 3 and 4). After one month, the wave front has reached the area where the meridional gradient of h_1 is the strongest (around 35°N), and an anomaly of opposite sign, whose amplitude is proportional to the initial anomaly, forms in the surface layer while the anomaly of h_2 keeps the same sign. The anomaly in the surface layer intensifies and propagates southward. This signal also extends slightly eastward but is not advected by the mean current. Note that the

formation of this anomaly does not prevent propagation of the coastal wave beyond the separation zone since it appears along the southern edge.

Because the viscosity remains weak, the propagation velocity of the modeled coastal wave matches that of a theoretical Kelvin wave. However, as the model has only a 1° resolution, its pattern is impaired. Indeed, gridpoint oscillation adds to the exponential decay normal to the coast. These oscillations have been filtered out using a running filter (in Figs. 3–7) in order to improve their visibility. Note, lastly, that an experiment similar to the previous one, but with an initial positive thickness anomaly, was performed. The results are identical to those described just above except that the signs of the response are reversed.

A similar experiment with a 1.5-layer model was also performed, with the thickness of the active layer equal to 900 m. As in the previous experiment, a coastal Kelvin wave forms and propagates around the basin.

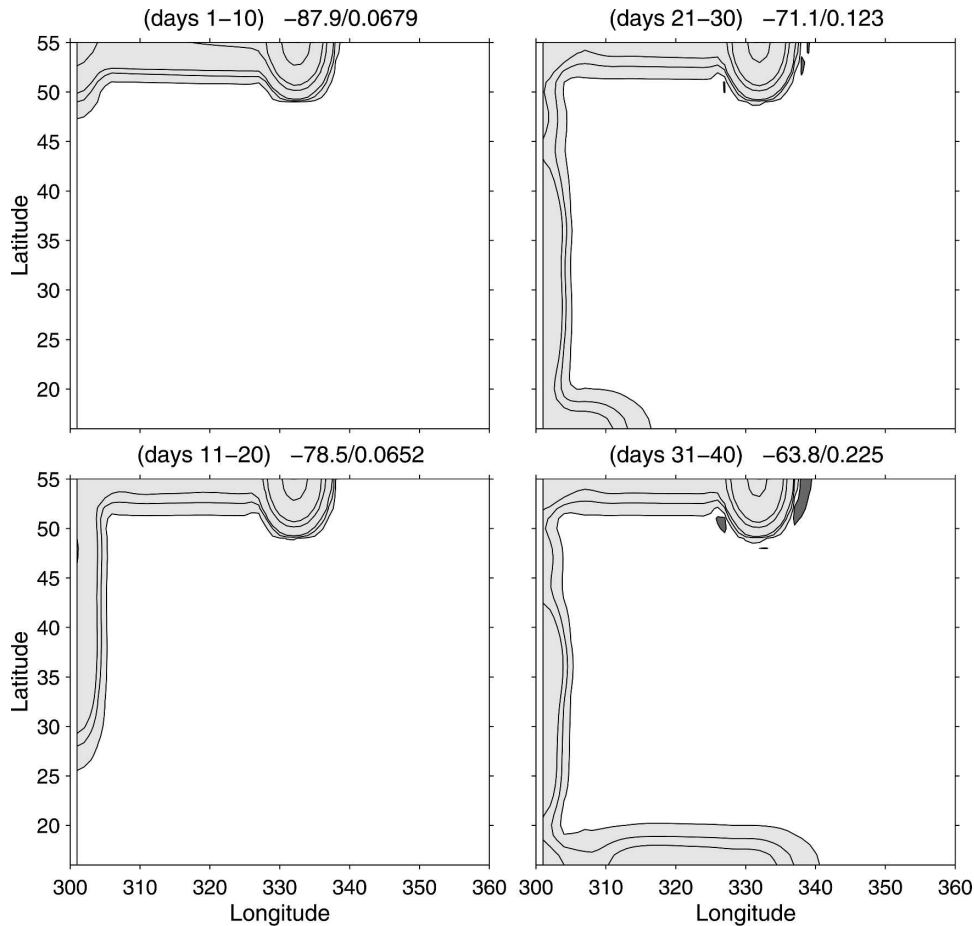


FIG. 4. As in Fig. 3 but for the anomalies of h_2 .

The anomaly associated with the wave keeps the same sign all around the basin and no anomaly of opposite sign forms in the separation area. This shows that two baroclinic modes are needed to form anomalies of opposite sign in the separation area of the western boundary current.

Experiments with prescribed mass flux between the layers have also been made. Those where the Kelvin wave induced by the mass flux has the same sign and approximately the same amplitude in both layers (first baroclinic mode) lead to similar results with the experiment where an initial thickness anomaly is applied. Such a wave may be generated, for example, by pumping water out of the midlayer into the layer at rest. Note that the dynamics in the area where the anomaly is generated becomes more complex because the perturbation applies during several months, which leads to a more noisy signal. The case where exchanges of mass occur between the active layers and Kelvin waves of the second baroclinic mode are excited has not been considered. It seems less realistic than the first one; indeed,

in the subpolar gyre the waves generated by temperature anomalies (mimicking deep convection) keep the same sign over more than 2000 m (see section 5).

3. Mechanism

Because the anomalies remain one or two orders of magnitude smaller than the mean values, the evolution of the perturbation in the separation area can be studied by linearizing the potential vorticity equations. Equation (3) becomes

$$\begin{aligned} \frac{\partial q'_i}{\partial t} + u_{i,S} \frac{\partial q'_i}{\partial x} + v_{i,S} \frac{\partial q'_i}{\partial y} + u'_i \frac{\partial q_{i,S}}{\partial x} + v'_i \frac{\partial q_{i,S}}{\partial y} = \\ - \frac{1}{h_{i,S}} \text{curl} \frac{h'_i (\tau_{i-1} - \tau_i)}{h_{i,S}^2} - \frac{h'_i}{h_{i,S}^2} \text{curl} \frac{(\tau_{i-1} - \tau_i)}{h_{i,S}} \\ + \frac{1}{h_{i,S}} \text{curl} \left(\nu \Delta_H \mathbf{v}'_i - \frac{\boldsymbol{\tau}'_i}{h_{i,S}} \right) \end{aligned} \quad (4)$$

(the prime indicates an anomaly and the subscript S indicates a mean value taken from the control experiment; cf. section 2).

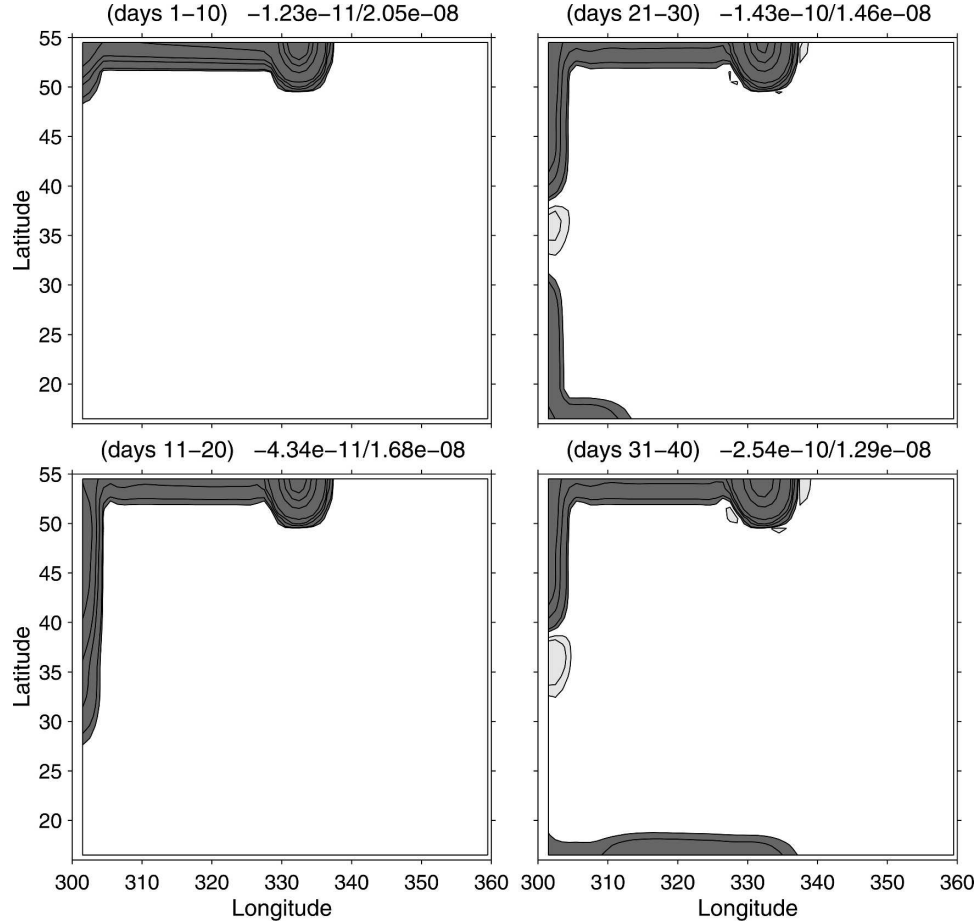


FIG. 5. Anomalies of the potential vorticity in the first layer of the 2.5-layer model (low resolution) at different times (as indicated in each panel). The 0 level is not indicated. The areas in dark gray are bounded by the isoline $0.5 \times 10^{-10} \text{ m}^{-1} \text{ s}^{-1}$ and contain isolines 1, 3, 5, 10, 50, 90, and 130 ($\times 10^{-10} \text{ m}^{-1} \text{ s}^{-1}$). The areas in light gray are bounded by the isoline $-0.5 \times 10^{-10} \text{ m}^{-1} \text{ s}^{-1}$ and contain isoline $-1 \times 10^{-10} \text{ m}^{-1} \text{ s}^{-1}$.

A scale analysis of the order of magnitude of the different terms in (4) for the surface layer, confirmed by the numerical results, indicates that $\partial_t q'_1$ is about $9.0 \times 10^{-17} \text{ m}^{-1} \text{ s}^{-2}$ (corresponding to an increase of the anomalous potential vorticity from 0 to $3.0 \times 10^{-9} \text{ m}^{-1} \text{ s}^{-1}$ over 1 yr), $u_{1,S} \partial_x q'_1 + v_{1,S} \partial_y q'_1$ is about $2.0 \times 10^{-16} \text{ m}^{-1} \text{ s}^{-2}$, and $u'_1 \partial_x q_{1,S} + v'_1 \partial_y q_{1,S}$ is about $3.0 \times 10^{-16} \text{ m}^{-1} \text{ s}^{-2}$, while the terms proportional to the wind stress τ_0 are about $5.0 \times 10^{-18} \text{ m}^{-1} \text{ s}^{-2}$ and those proportional to τ_1 are even smaller. Equation (4) can thus be simplified. For the surface layer, one obtains

$$\frac{\partial q'_1}{\partial t} + u_{1,S} \frac{\partial q'_1}{\partial x} + v_{1,S} \frac{\partial q'_1}{\partial y} = -u'_1 \frac{\partial q_{1,S}}{\partial x} - v'_1 \frac{\partial q_{1,S}}{\partial y} + (1/h_{1,S}) \text{curl}(\nu \Delta_H \mathbf{v}'_1), \tag{5}$$

which expresses the fact that the Lagrangian transport of potential vorticity anomalies by the mean flow [left-hand side of (5)] is mainly driven by the advection of the mean potential vorticity by the anomalous currents and dissipation [right-hand side of (5)].

In a linear approximation, the anomalous potential vorticity q'_1 is written as

$$q'_1 = \frac{\zeta'_1}{h_{1,S}} - \frac{h'_1}{h_{1,S}} q_{1,S}, \tag{6}$$

where $q_{1,S} = (\zeta_{1,S} + f)/h_{1,S}$. The mean potential vorticity is about $10^{-7} \text{ m}^{-1} \text{ s}^{-1}$ while the anomalous potential vorticity (6) is about $8 \times 10^{-10} \text{ m}^{-1} \text{ s}^{-1}$ and is largely dominated by the term $-q_{1,S} h'_1/h_{1,S}$. The anomalous potential vorticity q'_1 can thus be replaced by $-q_{1,S} h'_1/h_{1,S}$ in Eq. (5). Figure 5 shows the evolution of the

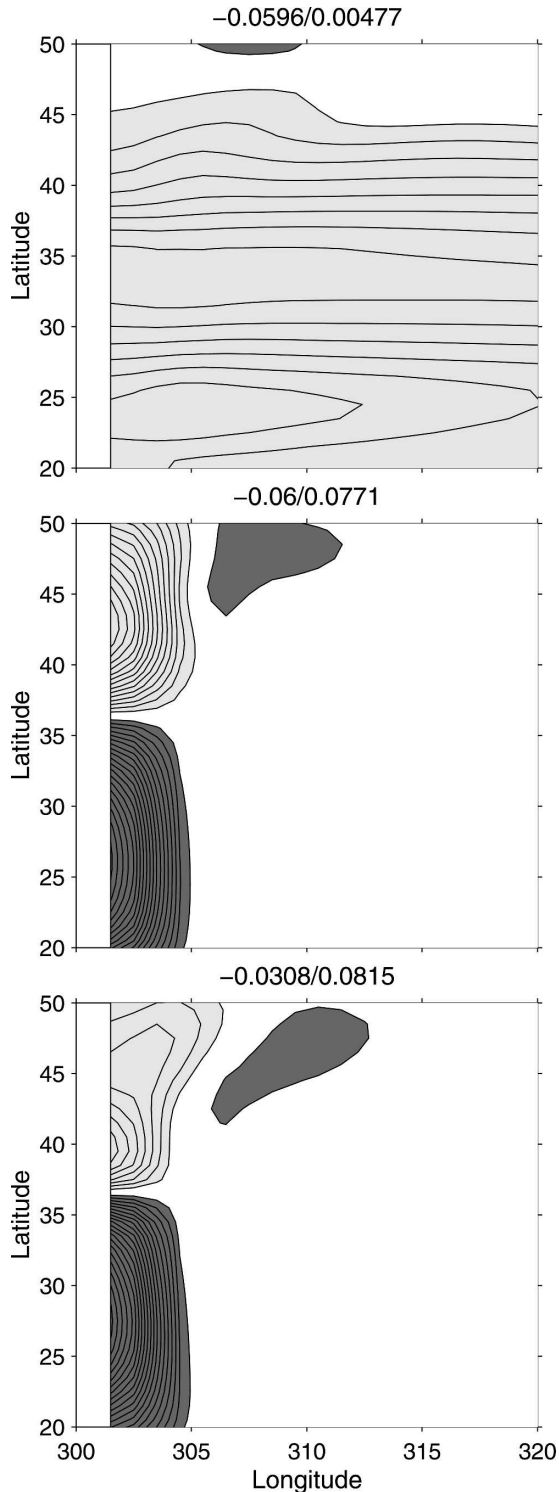


FIG. 6. Coefficients (top) A_u , (middle) A_v , and (bottom) λL with $L = 2000 \text{ km}$ (m s^{-1}). The zero line is not indicated and light (dark) gray is for negative (positive) values; interval between iso-lines is $4 \times 10^{-3} \text{ m s}^{-1}$.

anomalous potential vorticity, which, indeed, mimics that of the thickness (Fig. 3) with an opposite sign. As the system is nearly in geostrophic balance, u'_1 and v'_1 may be approximated by $-f^{-1}\partial_y(\alpha_1 b h'_1 + b h'_2)$ and $f^{-1}\partial_x(\alpha_1 b h'_1 + b h'_2)$. Considering these simplifications, Eq. (5) now reads

$$\partial_t h'_1 + A_u \partial_x h'_1 + A_v \partial_y h'_1 + \lambda h'_1 = \mathcal{F} + \mathcal{D}, \quad (7)$$

where

$$A_u = u_{1,S} - \frac{\alpha_1 b h_{1,S}}{f q_{1,S}} \partial_y q_{1,S},$$

$$A_v = v_{1,S} + \frac{\alpha_1 b h_{1,S}}{f q_{1,S}} \partial_x q_{1,S} \approx v_{1,S},$$

$$\lambda = (u_{1,S} \partial_x + v_{1,S} \partial_y) [\log(q_{1,S}/h_{1,S})],$$

$$\mathcal{F} = \frac{b h_{1,S}}{f q_{1,S}} (\partial_y q_{1,S} \partial_x h'_2 - \partial_x q_{1,S} \partial_y h'_2) \approx \frac{b h_{1,S}}{f q_{1,S}} \partial_y q_{1,S} \partial_x h'_2,$$

and \mathcal{D} represents the dissipative processes. Note that Eq. (7) can also be derived by linearizing around a mean flow (u_s, v_s) and then simplifying the equations of the 2.5 layer in quasigeostrophic approximation.

Though the details of Eq. (7) are complicated, its general form is simple: it combines advective effects in the zonal and meridional directions (terms $A_u \partial_x$ and $A_v \partial_y$), instability or damping effects following the sign of λ , forcing by the variations of the second layer thickness (term \mathcal{F}), and dissipative effects.

Figure 6 shows the coefficients A_u , A_v , and λ , which depend only on the mean state and constrain the evolution of the system. Since A_v is negative north and positive south of the separation area, the corresponding advective term simply transports the signal toward the separation area. Because A_u is everywhere negative, the term $A_u \partial_x$ will maintain the signal close to the western coast. Note that $u_{1,S}$ is positive, thus tends to advect the signal westward; but, A_u is dominated by $[(\alpha_1 b h_{1,S})/(f q_{1,S})] \partial_y q_{1,S}$ because of the strong gradient of mean potential vorticity. Last, since λ is negative (positive) north (south) of the separation area, it correspondingly increases (damps) the amplitude of the anomaly.

Figure 7 shows $-A_u \partial_x h'_1$, $-A_v \partial_y h'_1$, $-\lambda h'_1$, and \mathcal{F} , after two months of integration, when the anomaly of opposite sign is already well formed in the separation area (the plots are nearly identical after 15 days when the anomaly begins to appear, but with an amplitude divided by 4). As the anomaly increases, $\partial_t h'_1$ is mainly positive in the area and period of interest (not shown).

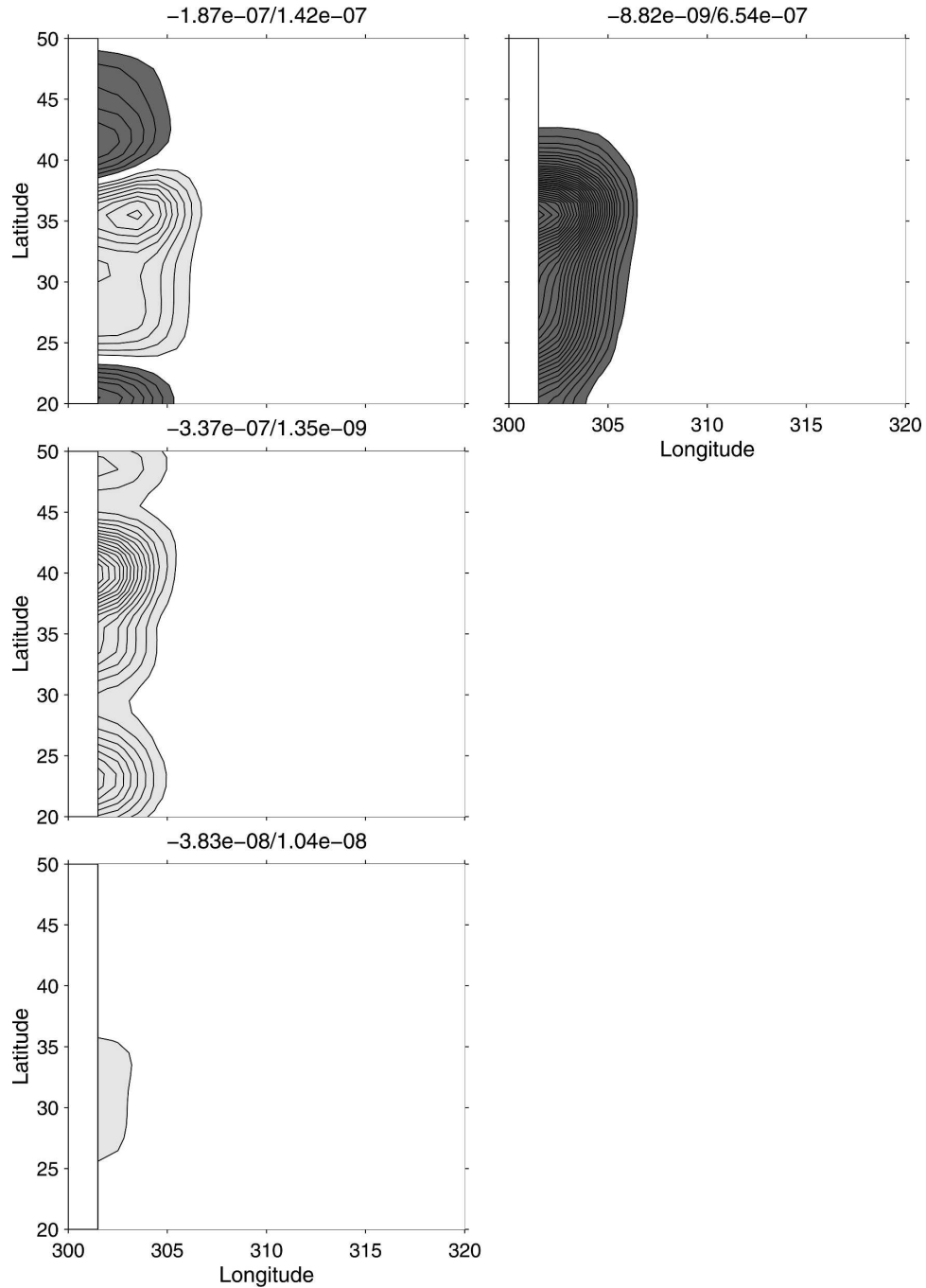


FIG. 7. Plots of (top) $A_u \partial_y h'_1$, (middle) $A_v \partial_y h'_1$, (bottom) $\lambda h'_1$, and (right) \mathcal{F} , 50 days after the start of the integration (m s^{-1}). The zero line is not indicated and light (dark) gray is for negative (positive) values; interval between isolines is $2 \times 10^{-8} \text{ m s}^{-1}$.

The forcing term \mathcal{F} , whose origin lies in the normal-to-shore gradient of the second-layer thickness due to the coastal Kelvin wave, is everywhere positive (this corresponds by geostrophy to a positive current anomaly); it thus tends to increase h'_1 , which ends up

taking a positive value. If the meridional gradient of mean potential vorticity in the separation area is small, \mathcal{F} remains small and no anomaly can form. The impact of the forcing term therefore strongly depends on the mean state.

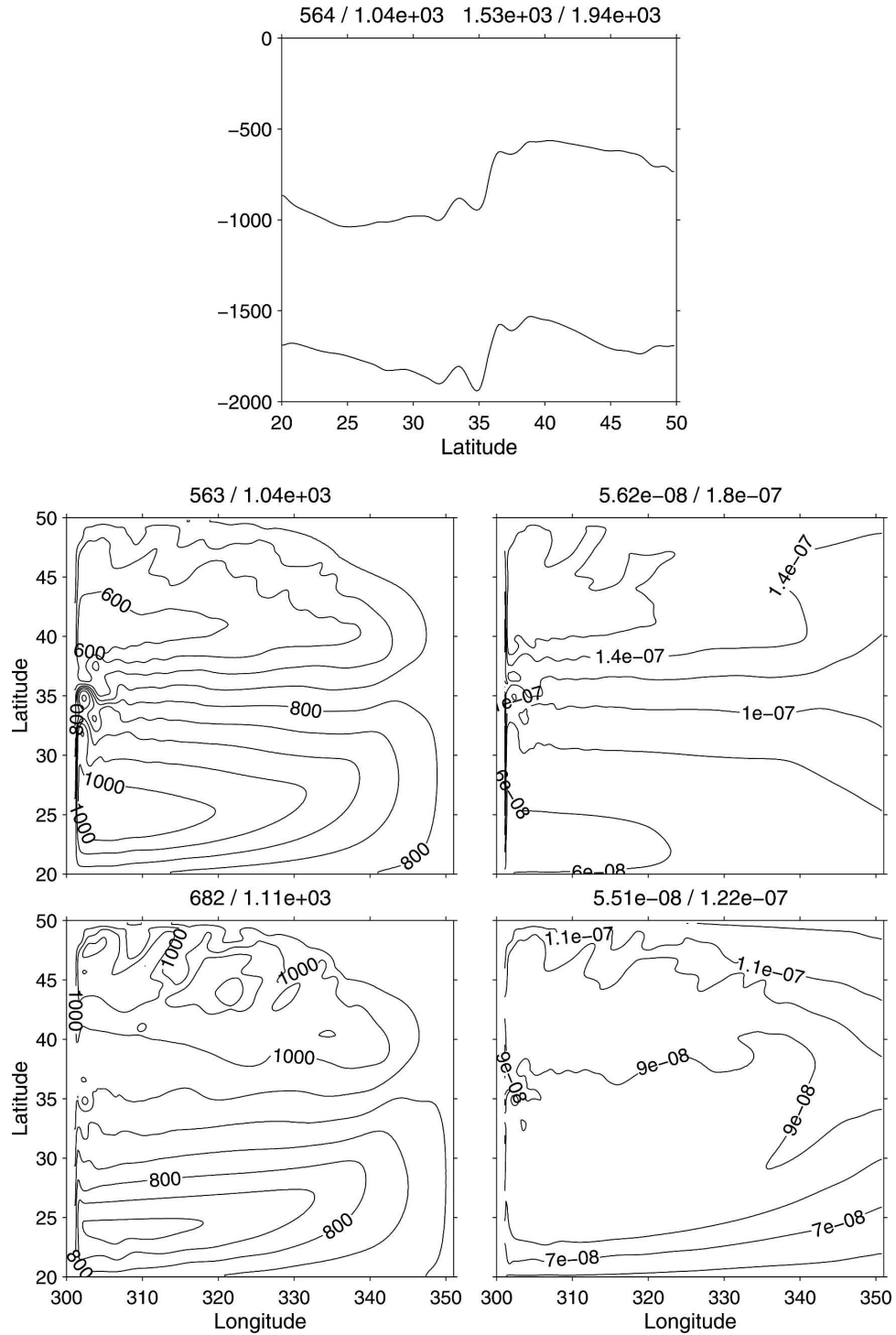


FIG. 8. As in Fig. 2 but for the high-resolution case.

The terms $-A_u \partial_x h'_1$ and $-A_v \partial_y h'_1$ are mainly negative and thus tend to slow down the increase of the positive anomaly in the separation area. Last, $-\lambda h'_1$ is an order of magnitude smaller than the others terms. Its role in

this configuration will therefore remain negligible. However, if the gradient of $q_{1,S}/h_{1,S}$ increases, a more important role should be expected.

To summarize, the basic ingredients to observe the

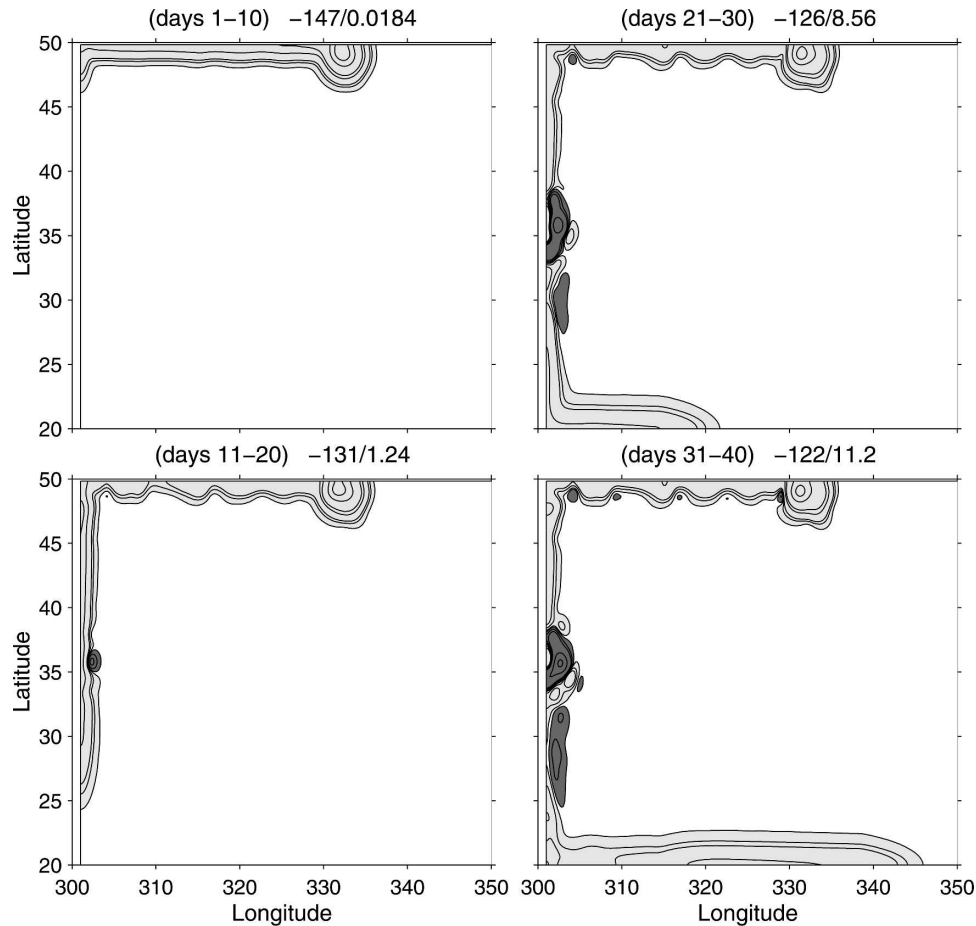


FIG. 9. Anomalies of h_1 in the 2.5-layer model (high resolution) at different times (as indicated in each panel); isolines are the same as in Fig. 3. A running filter has been applied to smooth small-scale patterns (below 1°).

formation of an anomaly of opposite sign in the intergyre region are

- i) the existence of two layers with contrasting properties, the variations of thickness of the lower layer acting as a forcing for the upper layer, and
- ii) a strong gradient of mean potential vorticity to ensure a strong response of the system and maintain the anomaly close to the coast (note that the reversal of the mean boundary currents in the separation area also forbids the anomaly to move northward or southward).

4. Study in a high-resolution configuration

In the high-resolution configuration, the mesh size of the model is set to $1/6^\circ$ and the domain is reduced to $60^\circ\text{--}10^\circ\text{W}$, $20^\circ\text{--}50^\circ\text{N}$ in order to reduce computational time. The viscosity coefficient ν is set to $100 \text{ m}^2 \text{ s}^{-1}$ (cf. Table 1). As the Rossby deformation radius is about 30

km at 50°N , the Kelvin waves are resolved in this configuration.

Figure 8 illustrates the mean state after 100 years of integration from rest. It is very similar to that obtained in the low-resolution case, but eddies are now present. They are mainly located along the northern coast and in the separation area. The depths of the interfaces show much stronger gradients than in the low-resolution experiment.

The initial thickness anomalies are now centered along the northern boundary at 49.5°N , 27.5°W . They have the same pattern and amplitude as in the low-resolution case. As illustrated in Fig. 9, a coastal Kelvin wave with the same sign in both layers still travels along the northern, then western, coasts. Its propagation velocity remains close to the theoretical value; since the wave is better resolved than previously, the signal is 4 times stronger. Eddies appear along the path of the wave, adding a small spatial scale signal. As in the low-

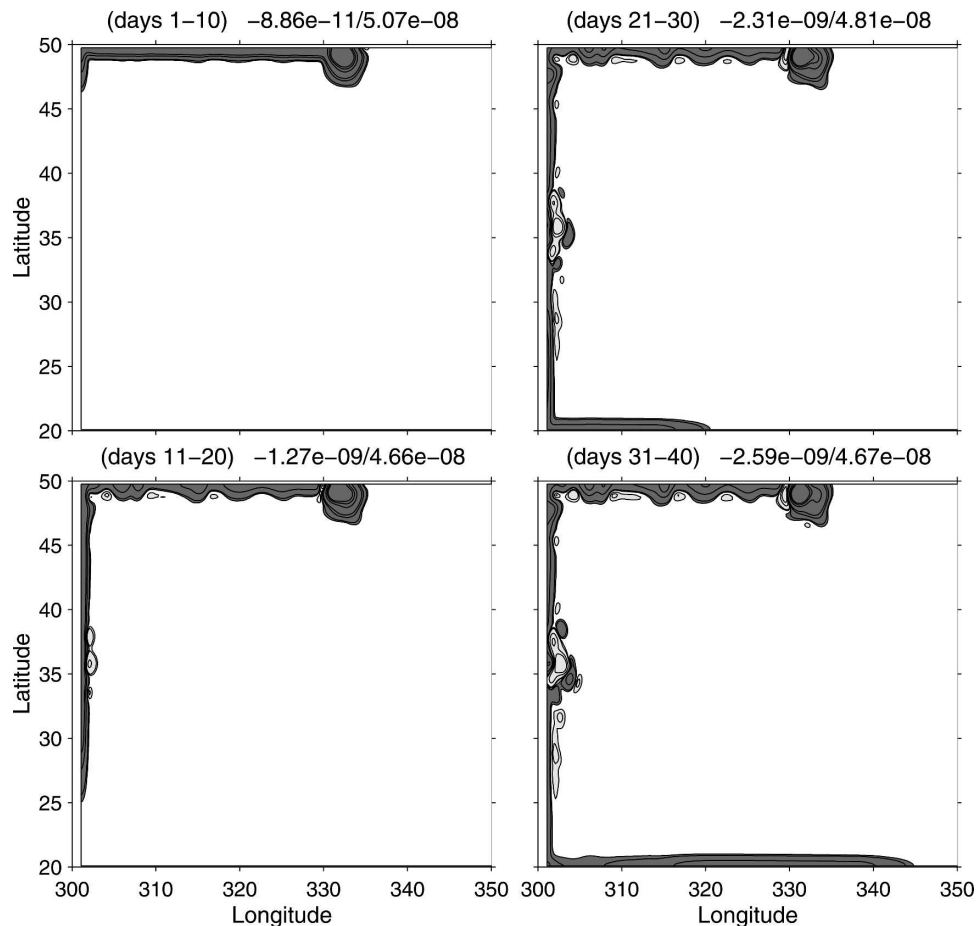


FIG. 10. Anomalies of the potential vorticity in the first layer of the 2.5-layer model (high resolution) at different times (as indicated in each panel). The 0 level is not indicated. The areas in dark gray are bounded by the isoline $0.5 \times 10^{-10} \text{ m}^{-1} \text{ s}^{-1}$ and contain isolines 1, 5, 10, 50, 90, and $130 \times 10^{-10} \text{ m}^{-1} \text{ s}^{-1}$. The areas in light gray are bounded by the isoline $-0.5 \times 10^{-10} \text{ m}^{-1} \text{ s}^{-1}$ and contain isolines -1, -5, and $-10 \times 10^{-10} \text{ m}^{-1} \text{ s}^{-1}$. A running filter has been applied to smooth small-scale patterns (below 1°).

resolution case, an anomaly of opposite sign forms in the surface layer in the separation area, but it has smaller spatial scales and a 4 times higher amplitude. The anomalous transport associated to the initial thickness anomaly is about 1 Sv ($\text{Sv} \equiv 10^6 \text{ m}^3 \text{ s}^{-1}$).

In this experiment, the anomaly of relative vorticity ζ'_1 has the same order of magnitude as the vorticity associated with the thickness variations of the first layer: $q_{1,s}h'_1$ [see Eq. (6)]. It thus equally contributes to the anomalous potential vorticity. When the anomalies are filtered on a scale larger than 1° , the anomalies of potential vorticity approximately follows those of h'_1 , with an opposite sign (Fig. 10). This suggests that the relative vorticity can be neglected and the relation between h'_1 and q'_1 obtained in the low-resolution case is still valid for spatial scales larger than those of the eddies; hence, though the eddies contain most of the kinetic energy of the signal at small spatial scale, they do

not notably modify the dynamics of the system on the large scale.

Figure 11 shows the forcing term \mathcal{F} [see Eq. (7)], which, as shown above, generates the sign change in the separation area. Its pattern is very similar to that obtained in Fig. 7, though there are more small spatial scales and the signal is stronger. This suggests that the mechanism described in section 3 subsists when the resolution is increased.

5. Response in a simple GCM

The previous experiments have been made with idealized models. To verify if a similar evolution and mechanism may be found in a more realistic context where the barotropic mode and several baroclinic modes are present, an experiment has been performed with an OGCM. The OGCM is the Massachusetts Institute of Technology (MIT) primitive equation model

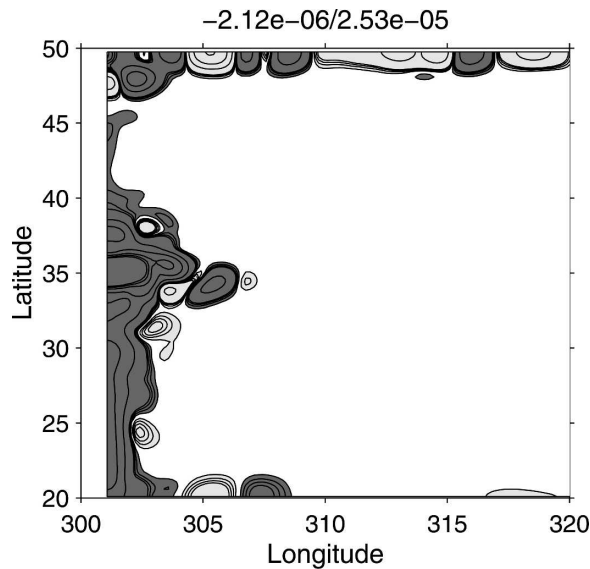


FIG. 11. Plot of ξ , 50 days after the start of the integration (m s^{-1}). The zero line is not indicated. The areas in light gray are bounded by isoline $-2 \times 10^{-8} \text{ m s}^{-1}$ and contain isolines $-4, -6, -8, -40,$ and $100 \times 10^{-8} \text{ m s}^{-1}$. The areas in dark gray are bounded by isoline $+2 \times 10^{-8} \text{ m s}^{-1}$ and contain isolines $+4, +6, +8, +40,$ and $+100 \times 10^{-8} \text{ m s}^{-1}$.

(Marshall et al. 1997) extending on a sphere from the equator to 60°N and from 60°W to 0° . The depth H is constant ($H = 4000 \text{ m}$). The horizontal resolution is $1^\circ \times 1^\circ$ (cf. Table 1). There are 10 levels in the vertical with 5 in the upper 600 m. The equation of state of seawater has the simplified form:

$$\rho = \rho_0[1 - \epsilon(T - T_{0,i})],$$

where $\epsilon = 2 \times 10^{-4} \text{ K}^{-1}$, $\rho_0 = 10^3 \text{ kg m}^{-3}$, and $T_{0,i}$ is a reference temperature that depends on the depth of layer i . The role of salinity is not considered. The horizontal eddy viscosity and thermal diffusivity are respec-

tively equal to 10^4 and $10^3 \text{ m}^2 \text{ s}^{-1}$. The vertical viscosity and diffusivity are respectively equal to 10^{-3} and $10^{-4} \text{ m}^2 \text{ s}^{-1}$, as in Cox (1985). Convection is parameterized by a nonpenetrative convective adjustment scheme when static instability occurs. No-slip boundary conditions are used and there is no bottom friction. The model has been spun up from rest for 540 years, whereupon a steady-state solution is achieved in the upper 1000 m. The idealized wind stress used for this spinup reproduces the observed tilt from southwest to northeast of the zero wind stress curl line. The surface heat flux is parameterized using the formula $Q_r = C_0(T_s - T_a)$, where $C_0 = 14.5 \text{ W m}^{-2} \text{ K}^{-1}$, T_s is the sea surface temperature, and T_a an idealized atmospheric temperature (for more details and figures, see HSF). Figure 12 shows the temperature at 300 m (left) and along the western coast (right). The western boundary current separates from the coast around 38°N , then flows northeastward along the $10^\circ\text{--}12^\circ\text{C}$ isotherms. A front around 40°N appears in the upper layers of the model (above 1000 m). It separates the subpolar gyre, where well-mixed waters are found, from the strongly stratified subtropical gyre.

Two 1-yr experiments based on this quasi-stationary state are performed: in the first, a constant temperature anomaly of -0.4°C is applied in the northeastern part of the basin over the upper 1000 m, whereas there is no anomaly in the second. Anomalies are defined from the differences between these two experiments so that the drift of the model is largely eliminated. The evolution of the temperature anomaly at 300 m is shown in Fig. 13. This variable has been chosen as a proxy to estimate the variations of the isopycnic surface depth. Indeed, a direct computation of the latter led to very noisy results. A coastal wave, whose amplitude is one order of magnitude smaller than the initial perturbation, propa-

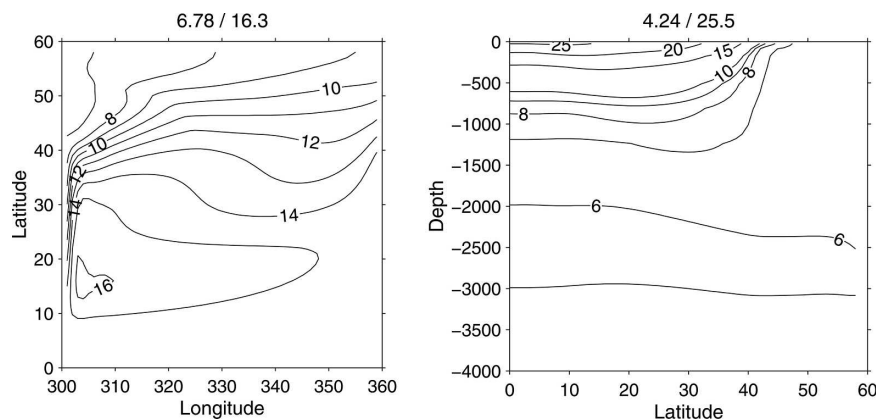


FIG. 12. Temperature at (left) 311 m and (right) along the western side in the GCM after a stationary state has been reached in the upper layers (above 1000 m).

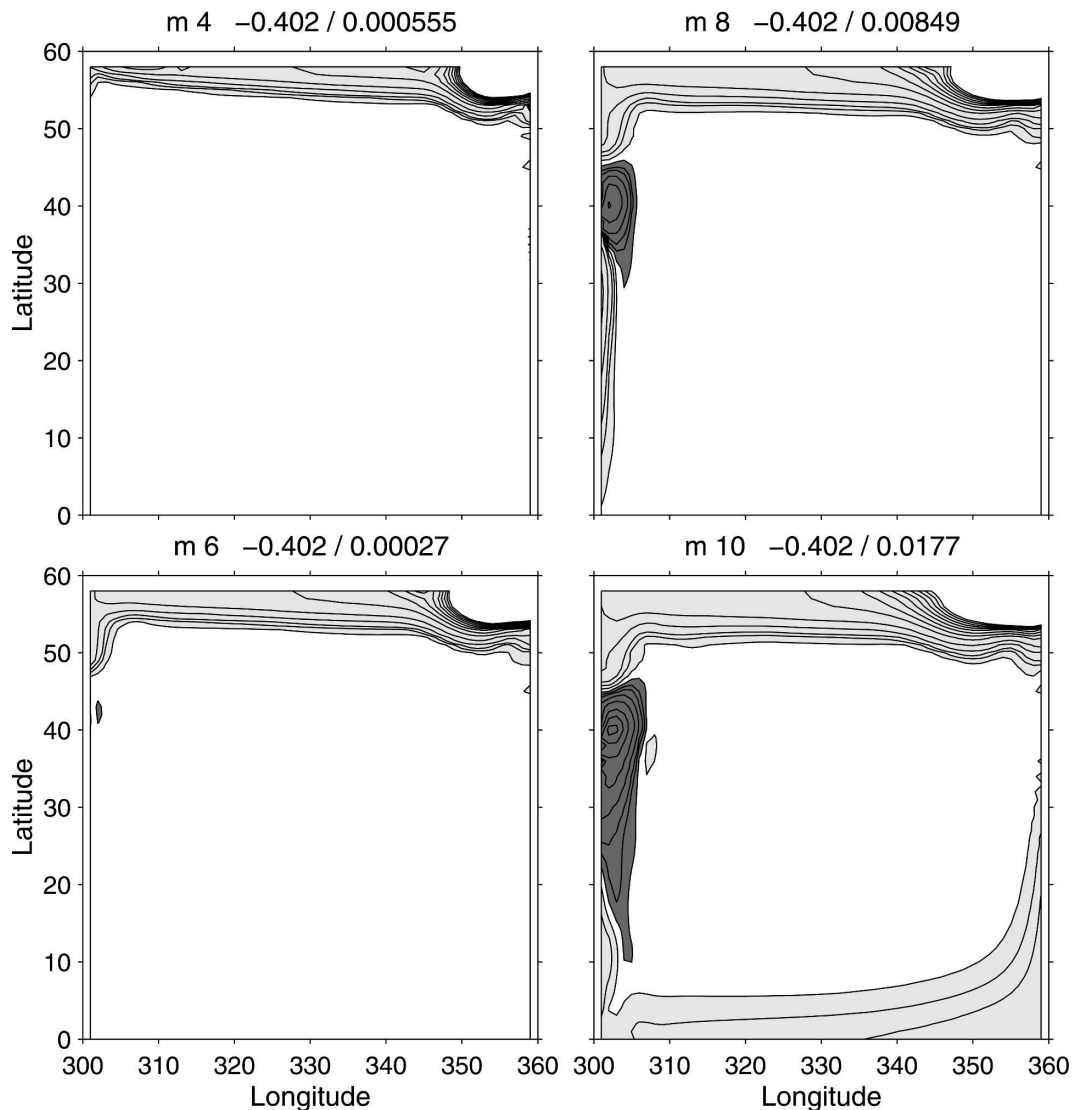


FIG. 13. Temperature anomalies ($^{\circ}\text{C}$) at 311 m in the MIT model. The anomalies are shown 4, 6, 8, and 10 months after the start of the integration. The 0 line is not drawn. The areas in dark gray are bounded by the isoline $2 \times 10^{-4} \text{ }^{\circ}\text{C}$ and contain isolines $+6, 10, 20, 40, 80, 120,$ and $160 \times 10^{-4} \text{ }^{\circ}\text{C}$. The areas in light gray are bounded by the isoline $-2 \times 10^{-4} \text{ }^{\circ}\text{C}$ and contain isolines $-6, -10, -20, -40, -80, -120, \dots \times 10^{-4} \text{ }^{\circ}\text{C}$.

gates along the northern, then western, coasts. This propagation can be detected up to 2000 m (not shown). As Kelvin waves are not resolved in this low-resolution model, the modeled wave does not have the same characteristics as theoretical Kelvin waves (emergence of an oscillatory behavior in the normal-to-coast direction). Its propagation velocity, which does not exceed 0.3 m s^{-1} , is weak mainly because of the strong viscosity (Hsieh et al. 1983; Davey et al. 1983). Following their computations, this high viscosity could explain a decrease of the propagation velocity by a factor of 4–5 with respect to the theoretical one in an inviscid model. This would lead, in this model, to a theoretical velocity

of about 1.3 m s^{-1} , which seems in agreement with the stratification along the northern boundary. After 6 months, the wave front reaches the area where the western boundary current separates from the coast. A temperature anomaly of opposite sign then begins to form south of the separation zone in the upper 1000 m. It increases during the following months and slowly extends southward along the western boundary. The upper part of the anomaly is advected eastward, above 200-m depth, by the mean flow (not shown). As in the previous experiments, the formation of the anomaly does not prevent the propagation of the coastal Kelvin wave beyond the separation area (see also Fig. 14).

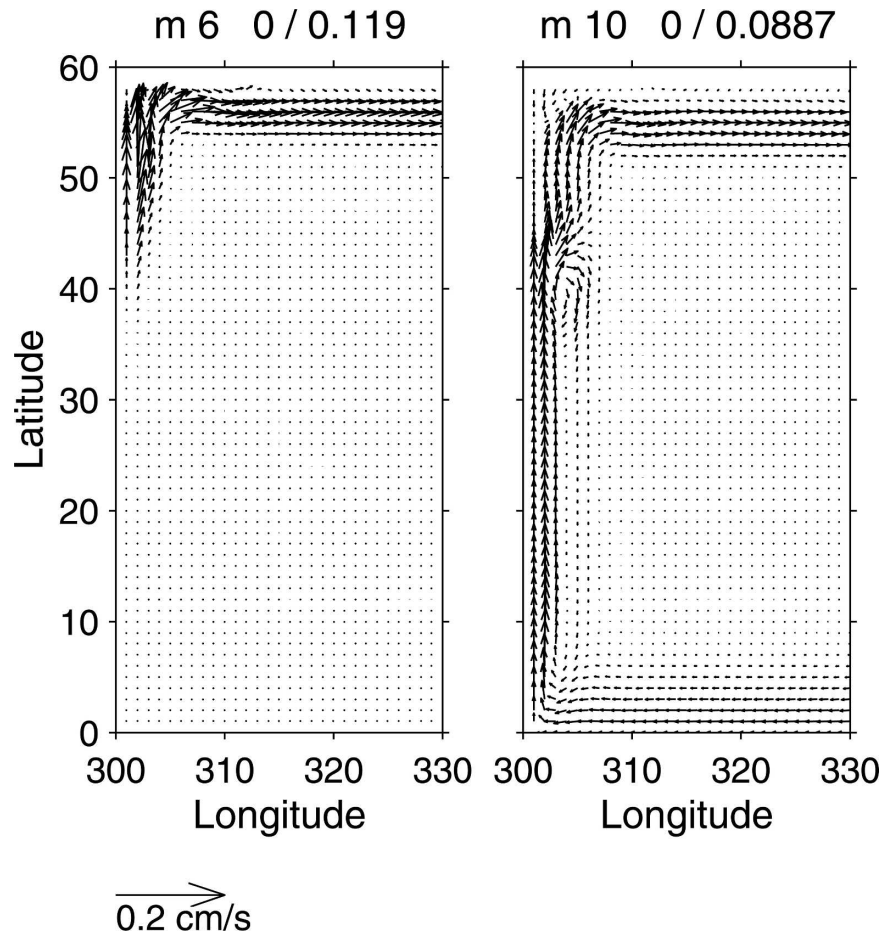


FIG. 14. Velocity anomalies (cm s^{-1}) at 311 m in the MIT model. The anomalies are shown 6 and 10 months after the start of the integration in the western part of the basin.

Figure 14 shows the velocity anomalies after 6 (left panel) and 10 (right panel) months of integration. Associated with the coastal wave, there is a current anomaly that flows northward along the western side. In the separation area, a clockwise whirling pattern forms simultaneously with the temperature anomaly.

The results are similar to those obtained with the layer models except that the anomaly formed in the separation area now propagates eastward in the upper layers. This is easily explained by the vertical shear of the current: in the surface layers $f\partial_z u$ is larger than $(g\delta\rho/\rho)\partial_y q_s/q_s$ (see the expression of A_u in section 3), and the effect of advection by the mean current dominates. On the other hand, below 200 m, the reverse occurs and the anomaly remains attached to the coast.

6. Conclusions

This paper considers the interaction of the Kelvin waves excited by deep water convection with the mean

circulation in the area where the Gulf Stream separates from the coast, and investigates it from numerical models of different complexity but simple geometry.

In all models, density anomalies produced close to the northern boundary generate coastal Kelvin waves that propagate toward the separation area. There, the sign of the anomaly formed behind the Kelvin front reverses in the surface layers (above 800–1000 m) while it keeps the same sign below. The mechanism of this sign change is the following: in the deepest layers, the Kelvin wave generates variations of thickness (or equivalently volume) that, in turn, create current anomalies acting as a forcing term on the upper layers. Since this forcing term is proportional to the gradient of mean vorticity, it is large enough to form an anomaly of opposite sign only in the separation area where the gradient of vorticity is the strongest. The growth of this anomaly is limited by the mean meridional currents. In the two-layer model, this anomaly remains close to the coast because the advection by the mean current is bal-

anced by the current anomalies due to the variations of thickness in the upper layer.

The presence of eddies does not seem to change significantly the nature of the response at spatial scales larger than the typical size of the eddies. Neither does a more realistic stratification. However, because the currents have a strong shear between the surface and subsurface layers, the anomaly that forms in the separation area is advected by the mean current in the upper layers (above 200-m depth).

The response to a density anomaly has been studied previously in configurations where the mean state of the ocean was assumed at rest, no wind stress being applied (e.g., Johnson and Marshall 2004; Deshayes and Frankignoul 2005). Consequently, the coastal Kelvin waves did not interact with the mean flow but propagated freely. Our study shows that, even if the Kelvin wave generates an anomaly in the separation area, the Kelvin wave is transmitted beyond this area without suffering any sign change. Moreover, its amplitude seems to weaken only slightly. Consequently, most of the results evidenced in these studies are certainly robust.

The oscillation found in HSF probably involves in a crucial way the mechanism described in this paper. Indeed, they found a coupling between the subtropical and subpolar gyre via temperature anomalies advected by the surface and subsurface currents in the subpolar gyre. This oscillation could add to that found by Spall (1996a,b); both oscillations have comparable time scales, but this study does not allow one to determine if one mechanism is dominant in comparison with another.

Acknowledgments. We thank Claude Frankignoul for stimulating discussions. We thank the reviewers for their comments, which were helpful in improving the manuscript. This work is supported by the EU Framework 6 Programme under Contract 003903-GOCE (DYNAMITE). Computations have been done at the Institut du Développement et des Ressources en Informatique Scientifique.

REFERENCES

- Broecker, W., and G. H. Denton, 1989: The role of ocean-atmosphere reorganizations in glacial cycles. *Geochim. Cosmochim. Acta*, **53**, 2465–2501.
- Cox, M. D., 1985: An eddy resolving numerical model of the ventilated thermocline. *J. Phys. Oceanogr.*, **15**, 1312–1324.
- Davey, M. K., W. W. Hsieh, and R. Wajsoiwicz, 1983: The free Kelvin wave with lateral and vertical viscosity. *J. Phys. Oceanogr.*, **13**, 2182–2191.
- Deshayes, J., and C. Frankignoul, 2005: Spectral characteristics of the response of the meridional overturning circulation to deep-water formation. *J. Phys. Oceanogr.*, **35**, 1813–1825.
- Dong, B.-W., and R. T. Sutton, 2001: The dominant mechanisms of variability in Atlantic Ocean heat transport in a coupled ocean-atmosphere GCM. *Geophys. Res. Lett.*, **28**, 2445–2448.
- Eden, C., and J. Willebrand, 2001: Mechanism of interannual to decadal variability of the North Atlantic general circulation. *J. Climate*, **14**, 2266–2280.
- Herbaut, C., J. Sirven, and S. Février, 2002: Response of a simplified oceanic general circulation model to idealized NAO-like stochastic forcing. *J. Phys. Oceanogr.*, **32**, 3182–3192.
- Hsieh, W. W., M. K. Davey, and R. Wajsoiwicz, 1983: The free Kelvin wave in finite difference numerical models. *J. Phys. Oceanogr.*, **13**, 1383–1397.
- Huang, R. X., M. A. Cane, N. Naik, and J. Goodman, 2000: Global adjustment of the thermocline in response to deepwater formation. *Geophys. Res. Lett.*, **27**, 759–762.
- Johnson, H. L., and D. P. Marshall, 2002: A theory for the surface Atlantic response to thermohaline variability. *J. Phys. Oceanogr.*, **32**, 1121–1132.
- , and —, 2004: Global teleconnections of meridional overturning circulation anomalies. *J. Phys. Oceanogr.*, **34**, 1702–1722.
- Kawase, M., 1987: Establishment of deep ocean circulation driven by deep-water production. *J. Phys. Oceanogr.*, **17**, 2294–2317.
- Manabe, S., and R. J. Stouffer, 1994: Multiple-century response of a coupled ocean-atmosphere model to an increase of atmospheric carbon dioxide. *J. Climate*, **7**, 5–23.
- Marshall, J., A. Adcroft, C. Hill, L. Perelman, and C. Heisey, 1997: A finite volume, incompressible Navier Stokes model for studies of the ocean on parallel computers. *J. Geophys. Res.*, **102**, 5753–5766.
- Mauritzen, C., and S. Häkkinen, 1999: On the relationship between dense water formation and the “Meridional Overturning Cell” in the North Atlantic Ocean. *Deep-Sea Res. I*, **46**, 877–894.
- Sadourny, R., 1975: The dynamics of finite difference models of the shallow water equations. *J. Atmos. Sci.*, **32**, 680–689.
- Schott, F., R. Zantopp, L. Stramma, M. Dengler, J. Fischer, and M. Wibaux, 2004: Circulation and deep-water export at the western exit of the subpolar North Atlantic. *J. Phys. Oceanogr.*, **34**, 817–843.
- Sirven, J., 1996: The equatorial undercurrent in a two layer shallow water model. *J. Mar. Syst.*, **9**, 171–186.
- Spall, M. A., 1996a: Dynamics of the Gulf Stream/deep western boundary current crossover. Part I: Entrainment and recirculation. *J. Phys. Oceanogr.*, **26**, 2152–2168.
- , 1996b: Dynamics of the Gulf Stream/deep western boundary current crossover. Part II: Low-frequency internal oscillations. *J. Phys. Oceanogr.*, **26**, 2169–2182.
- Wajsoiwicz, R. C., and A. E. Gill, 1986: Adjustment of the ocean under buoyancy forces. Part I: The role of Kelvin waves. *J. Phys. Oceanogr.*, **16**, 2097–2114.